Dalton Transactions

ROYAL SOCIETY OF CHEMISTRY

PAPER

View Article Online
View Journal

Cite this: DOI: 10.1039/d5dt01166c

Transition metal-doped porous carbon nitride composites serve as highly reactive catalysts for thermal decomposition of ammonium perchlorate†

Qin Liu,‡[a] Siyu Ma,‡[b] Xingyang Cui,[a] Shuyue Xu,[a] Jinchao Ma *[a] and Hua Qian*[a]

Received 18th May 2025,
Accepted 8th July 2025

DOI: 10.1039/d5dt01166c

rsc.li/dalton

The performance of composite solid propellants (CSPs) is influenced by the energy release rate and combustion efficiency of ammonium perchlorate (AP), which serves as their core oxidizer. In this research, porous carbon nitride-based composites doped with transition metals (Mn, Fe, Co, Ni, and Cu) (PCN-M) were rapidly fabricated through precipitation and low-temperature calcination, and were comprehensively characterized. It was found that such additives are conducive to regulating the thermal decomposition pathway of AP and enhancing the combustion efficiency of propellants. The results demonstrate that among the prepared composite materials, PCN-0.5Co exhibits optimal catalytic performance: addition of 5 wt% PCN-0.5Co can reduce the high-temperature decomposition temperature (HTD) of AP by 125.71 °C, lower the apparent activation energy (E_a) to 113.04 kJ mol^{-1}, and shorten the thermal decomposition time by 45.13%. Furthermore, when 2 wt% PCN-2.0Co was applied to HTPB-based solid propellants, the results showed that its thermal decomposition peaks merged into a single exothermic peak, the HTD temperature decreased by 53.5 °C, the combustion rate increased by 39.40% (1.355 mm s^{-1}), and the heat of explosion increased to 4996 J g^{-1}. This study provides novel ideas for the design of high-performance AP combustion catalysts and the application of carbon nitride-based materials in solid propulsion engineering.

1. Introduction

Composite solid propellants (CSPs), serving as the primary energy source for solid rocket motors, have garnered significant attention due to their high energy density, storage stability, and reliable ignition performance. These propellants are typically formulated with oxidizers, metallic fuel, polymer binders, and functional additives. Their combustion efficiency and energy release characteristics are critically dependent on the thermal decomposition behavior of their core oxidizer – ammonium perchlorate (AP).[1–6] However, AP's practical application faces substantial challenges due to its elevated thermal decomposition temperature (HTD > 400 °C), sluggish decomposition kinetics, and incomplete combustion characteristics. These inherent limitations lead to restricted burning rates and energy losses in propellant systems, ultimately posing critical barriers to the development of high-performance CSPs.[7–10]

The incorporation of low-load catalysts represents an effective strategy to optimize the decomposition of AP.[11–17] Transition metal nanoparticles (TMNs) have been widely used in the catalytic decomposition of ammonium perchlorate (AP) due to their unique 3d orbital configurations and large specific surface areas.[5,18,19] Among them, transition metal oxides such as Co_3O_4,[20] Fe_2O_3,[21] CuO,[22] and NiO[23] have attracted significant attention because of their stable physicochemical properties and high catalytic activity. For example, Li *et al.*[24] investigated the effect of nano-CuO particles with different microstructures prepared under various conditions on the thermal decomposition of AP. The nano-CuO synthesized using NaOH showed the best catalytic performance—reducing the high-temperature decomposition peak of AP from 453.02 °C to 325.51 °C and increasing the total exothermic heat from 575.48 J g^{-1} to 1293.47 J g^{-1}. Chen *et al.*[25] prepared Co_3O_4 with a hollow double-shell structure, whose hierarchical mor-

---

[a] School of Chemistry and Chemical Engineering, Nanjing University of Science and Technology, Nanjing 210094, P.R. China. E-mail: mjinchao@njust.edu.cn, qianhua@njust.edu.cn

[b] Shanghai Space Propulsion Technology Research Institute, Shanghai, 201109, P.R. China

† Electronic supplementary information (ESI) available. See DOI: https://doi.org/10.1039/d5dt01166c

‡ These authors contributed equally.

phology, large surface area, and unique electronic structure endowed it with excellent catalytic activity for AP decomposition—lowering the decomposition temperature to 318 °C and increasing the exothermic heat from 491 J g^{-1} to 1280 J g^{-1}. However, in practical applications, nano-metal particles tend to agglomerate, significantly reducing their specific surface area and catalytic activity,[3,26–30] which severely restricts the application of TMNs in AP catalysis.

To prevent agglomeration of nanoparticles, carbon materials with high specific surface areas such as graphene,[31] graphene oxide,[32] carbon nanotubes,[33] graphitic carbon nitride,[34] and carbon black[35] can be employed as supports to decorate nanoscale transition metal particles. Carbon-supported nanocomposites integrate the merits of nanoscale transition metal particles and carbon-based materials, demonstrating excellent catalytic performance.[36] In particular, catalysts derived from carbon nitride materials have become a research hotspot recently.[23,27,34,37,38] In our previous research, porous carbon nitride (PCN, $C_{3.00}N_{4.45}H_{0.22}O_{0.88}$), due to its special molecular structure and morphology, exhibited remarkable catalytic activity.[39] However, the synergistic effect of the porous carbon nitride support and transition metals remains underexplored. Therefore, PCN is selected as the carbon-based support, and transition metals are loaded onto it, with the aim of fabricating combustion catalysts with excellent catalytic performance and investigating the mechanism of their synergistic catalysis.

In summary, this study presents a novel strategy to fabricate transition metal-doped porous carbon nitride composites (PCN-M) as efficient catalysts for AP thermal decomposition. Unlike conventional single-component metal oxides or undoped carbon supports, the PCN-0.5Co composite achieves unprecedented catalytic performance, evidenced by a 125.71 °C reduction in AP's high decomposition temperature and a 58.2% decrease in activation energy compared to pristine AP. This performance stems from the synergistic effect of PCN's high-surface-area porous framework and the redox activity of cobalt species, which promotes efficient adsorption of AP decomposition intermediates (*e.g.*, $HClO_4$) and accelerates reactive oxygen species (O^-) generation. Notably, when 2 wt% PCN-2.0Co is applied to HTPB-based solid propellants, it merges decomposition peaks into a single exothermic event, lowers the high-temperature decomposition temperature by 53.5 °C, and increases the combustion rate by 39.4% (1.355 mm s^{-1}).

2. Experimental section

2.1 Starting materials

The compounds $Mn(NO_3)_2·4H_2O$ (99.7%), $Fe(NO_3)_2·9H_2O$ (99.7%), $Co(NO_3)_2·6H_2O$ (99.7%), $Ni(NO_3)_2·6H_2O$ (99.7%), $Cu(NO_3)_2·3H_2O$ (99.7%), nano-Co_3O_4 (99.5%, 30 nm) and AP (99.7%) were procured from Shanghai Aladdin Biochemical Technology Co., Ltd. Aluminum powder (Al, 99.7%, 100–200 mesh) was purchased from Sinopharm Chemical Reagent Co., Ltd. Hydroxyl-terminated polybutadiene (HTPB) characterized by a hydroxyl value of 0.65–0.70 mmol g^{-1}, toluene diisocyanate (TDI, 98%), and dibutyltin dilaurate (T12, 98%) were procured from Shanghai Meryer Biochemical Technology Co., Ltd. The precursor for polymeric carbon nitrides (PCNs) was synthesized following a method previously documented in the literature.[39] All chemical reagents were used directly without any purification.

2.2 Preparation of PCN-M

Nitrogen-doped carbon-based nanocomposites were synthesized *via* precipitation and low-temperature calcination, designated as PCN-M (where M = Mn, Fe, Co, Ni, and Cu) (Fig. 1). The general procedure for the preparation of PCN-M is outlined as follows: 0.0987 g of PCN powder (Fig. S1†) was added in an aqueous solution of 0.5 mmol $Mn(NO_3)_2·4H_2O$, $Fe(NO_3)_2·9H_2O$, $Co(NO_3)_2·6H_2O$, $Ni(NO_3)_2·6H_2O$ or $Cu(NO_3)_2·3H_2O$, respectively. Subsequently, 10 mL of 1 mol L^{-1} NaOH solution was slowly added, under continuous stirring for 2 hours at room temperature. The solid product was filtered, washed, and dried at 50 °C. The obtained precursor was then calcined in a muffle furnace at 200 °C for 3 h, yielding a metal-doped carbon nitride composite (PCN-M). To quantitatively analyse the metal loading effects on the catalyst's architecture and performance, a series of PCN-*x*M composites (x = 0.25, 0.5, 1.0, and 2.0 mmol) were fabricated across a concentration gradient by precisely controlling metal precursor loadings (Mn, Fe, Co, Ni, and Cu).

2.3 Characterization

A Fourier transform infrared (FTIR) spectrometer (Bruker INVENIO) was employed to investigate the chemical bonding of the samples within the wavenumber range of 4000 to 400 cm^{-1}. The phase composition of the samples was analyzed using an X-ray diffractometer (XRD, Bruker AXS D8 Advance). The micromorphology and elemental distribution of the PCN-M composites were characterized using a scanning electron microscope (SEM, Hitachi Regulus 8100) in conjunction with an energy dispersive X-ray spectrometer (EDS) at an accelerated voltage of 10.0 kV. A transmission electron microscope (TEM, FEI-Tecnai12) was used to examine the internal structure of the samples at an accelerated voltage of 120 kV. The composition and structural characteristics of the samples were further analyzed using X-ray photoelectron spectroscopy (XPS, Thermo Fisher Nexsa). The specific surface area, pore volume, and pore size distribution of the samples were determined through the Brunauer–Emmett–Teller (BET) method (Micromeritics ASAP 2460), with the pore structure type assessed *via* nitrogen adsorption–desorption isotherms. The explosion heat of the samples was measured using a bomb calorimeter (PARR 6200) under an argon pressure of 3.0 MPa.

2.4 Catalytic activity measurement

To evaluate the catalytic effects of various catalysts on the thermal decomposition of AP, a series of composite mixtures were prepared, each containing a consistent concentration of 5 wt% catalyst. The preparation protocol involved the combi-

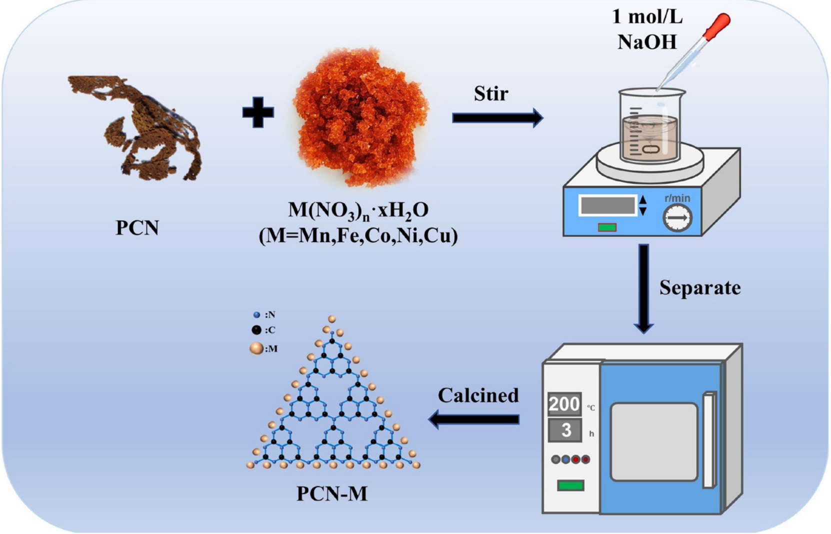

Fig. 1 Schematic diagram of the process of preparing PCN-M composites by the low-temperature calcination method.

nation of 50 mg of the catalyst with 950 mg of AP, followed by the addition of acetone. The resulting mixture was then ground in an agate mortar for 30 minutes. After the drying phase, the catalytic performance was evaluated through thermogravimetric analysis combined with differential scanning calorimetry (TG-DSC, Mettler Toledo TGA/DSC 3+). To further investigate the catalytic mechanism of PCN-M on the thermal decomposition of AP, differential scanning calorimetry (DSC, Mettler Toledo DSC 3) was employed to conduct tests at varying heating rates of 5, 10, 15, and 20 K min^{-1}. Additionally, the gaseous products generated during the catalytic decomposition of AP were monitored in real-time using a TG-FTIR system (Mettler Toledo TGA-Nicolet IS50), under conditions that were consistent with those used in the assessment of catalytic performance.

2.5 Propellant combustion performance measurement

The standard formulation for the HTPB-based solid propellant comprises 68% AP, 18% aluminum, 12% HTPB, 1.5% TDI, and 0.5% T12. The particle size of the AP used is shown in Fig. S35,† with an average particle size of 134.3 μm. A mixture consisting of 1.8 g of HTPB, 0.225 g of TDI, and 0.075 g of T12 was blended for five minutes. Simultaneously, 10.2 g of AP and 2.7 g of aluminum powder were mixed separately for ten minutes to ensure a uniform powder consistency. Following this, 0.3 g (2 wt%) of catalyst was added to the AP–Al powder mixture and thoroughly integrated. The resulting powder mixture was then combined with the HTPB–TDI–T12 mixture and agitated for forty minutes. The final solid propellant slurry was cast into a glass mold with an inner diameter of 9 mm, which had previously incorporated a bundle of nickel–chromium ignition wires at the base. The assembly underwent vacuum treatment for thirty minutes and was subsequently cured at 50 °C for forty-eight hours, resulting in the production of the final HTPB-based solid propellant beam.

3. Results and discussion

3.1 Characterization of samples

The X-ray diffraction (XRD) patterns of PCN and PCN-M composites are shown in Fig. 2a. The presence of a broad diffraction peak at 26.17° for the unmodified PCN indicates its amorphous structure. All PCN-M composites maintain the primary diffraction peak of PCN at 26.17° with no measurable shifts, confirming that transition metal doping does not induce significant lattice distortion. This is attributed to the low metal loading, uniform dispersion, and the amorphous nature of the PCN framework.[40] Among them, PCN-0.5Mn exhibits four distinct characteristic diffraction peaks at 32.38°, 36.08°, 58.50°, and 59.91°, corresponding to the (013), (211), (321), and (224) crystal planes of Mn_3O_4, respectively.[41] PCN-0.5Fe shows four distinct characteristic diffraction peaks at 21.09°, 33.06°, 52.93°, and 58.74°, which can be assigned to the (110), (130), (221), and (151) crystal planes of FeO(OH), respectively.[42] PCN-0.5Co presents three distinct characteristic diffraction peaks at 20.24°, 37.01°, and 38.93°, corresponding to the (003), (101), and (012) crystal planes of CoO(OH), respectively.[43] PCN-0.5Ni exhibits four distinct characteristic diffraction peaks at 19.15°, 33.02°, 38.45°, and 58.97°, which are attributed to the (001), (100), (011), and (110) crystal planes of $Ni(OH)_2$, respectively.[44] PCN-0.5Cu shows two distinct characteristic diffraction peaks at 35.39° and 38.29°, corresponding to the (−111) and (111) crystal planes of CuO, respectively.[45]

As illustrated in Fig. 2b, the FTIR spectra of PCN and PCN-M composites exhibit distinct vibrational modes starting with a broad absorption band at 3200 cm^{-1}, which is assigned to the N–H stretching of uncondensed terminal amine groups ($-NH_2$ or $=NH$).[46–48] Moving to lower wavenumbers, a series of peaks at 1260, 1315, 1400 and 1630 cm^{-1} correspond to the characteristic stretching modes of CN heterocycles, indicating the formation of a C–N═C bond extension network.[49–51] The

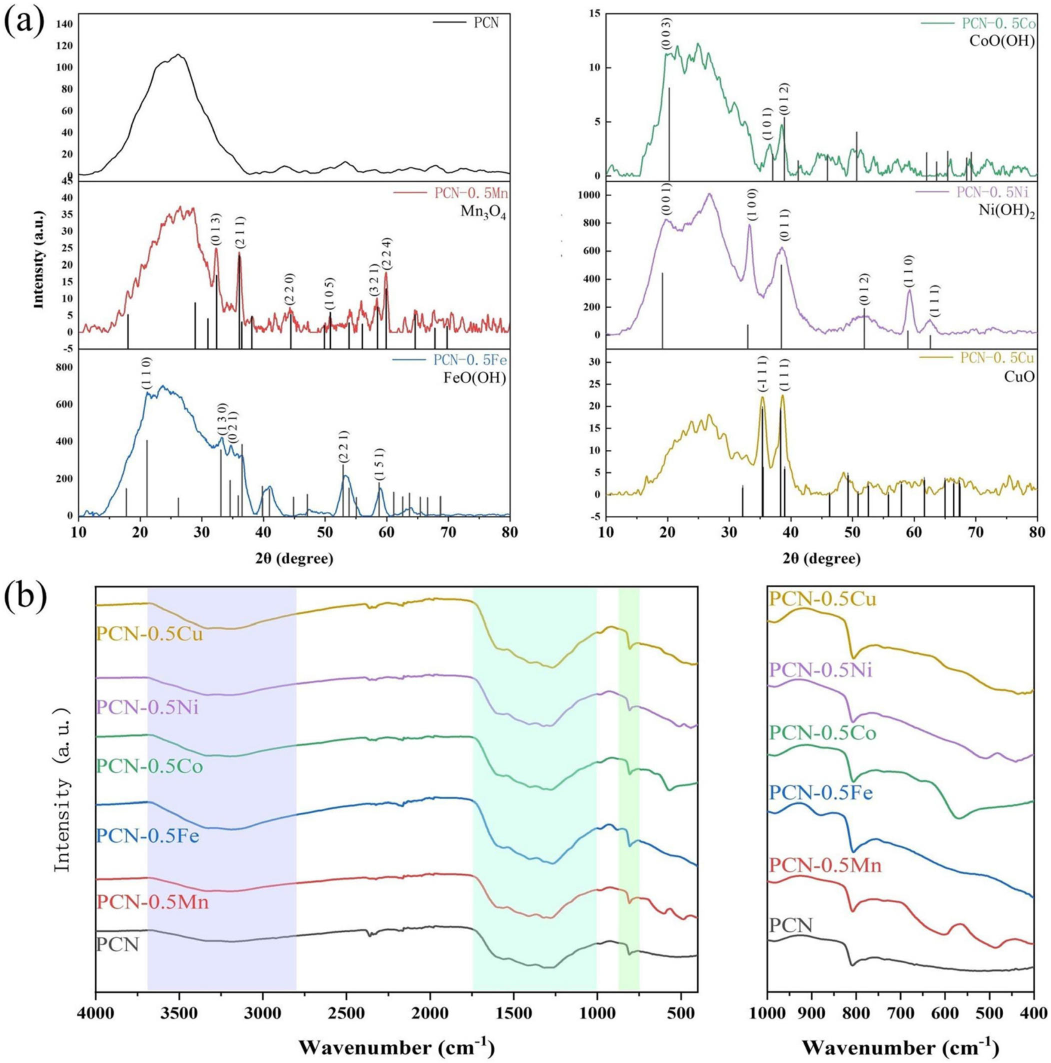

Fig. 2 XRD patterns (a) and FTIR spectra (b) of PCN and PCN-M.

sharp band at 807 cm^{-1} is attributed to the out-of-plane bending vibration characteristics of triazine units.[52–54] Importantly, the PCN-M composites display nearly identical skeletal vibration patterns to those of pristine PCN, indicating that the incorporation of metal does not compromise the integrity of the host framework, which is consistent with the structural observations obtained from X-ray diffraction (XRD).

The morphology of PCN-0.5Co was analyzed by scanning electron microscopy (SEM) and transmission electron microscopy (TEM) (Fig. 3 and Fig. S8, S9, ESI†). Representative SEM images of PCN-0.5Co (Fig. 3a) illustrate the amorphous structure with a rough surface texture and relatively uniform encapsulation of metallic components throughout the PCN substrate.[21] This morphology is consistent with the low-temperature calcination synthesis route, where metal nanoparticles are anchored on the PCN surface without causing significant aggregation, as previously reported for carbon nitride-supported metal composites. The rough surface texture, attributed to the porous framework of PCN, facilitates metal dispersion and enhances active site exposure, in line with SEM observations of similar hybrid materials.[37] Elemental mapping (Fig. 3a inset) confirms the homogeneous distribution of C, N, and Co, further validating the composite structure.[23] SEM-EDS analyses were extended to other PCN-M composites (M = Mn, Fe, Ni, and Cu) to verify the universality of the synthesis strategy. As shown in Fig. S10–S23 (ESI†), all samples exhibit amorphous morphologies with rough surface textures, similar to PCN-0.5Co. EDS mapping confirms the homogeneous distribution of metal elements (Mn, Fe, Ni, and Cu) on the PCN matrix, with no obvious aggregation, indicating that the low-temperature calcination method enables uniform metal loading across different transition metals. TEM analysis (Fig. 3b and c) further supports this structural configuration, revealing low electron transparency that confirms the homogeneous distribution of cobalt species on the surface of PCN.

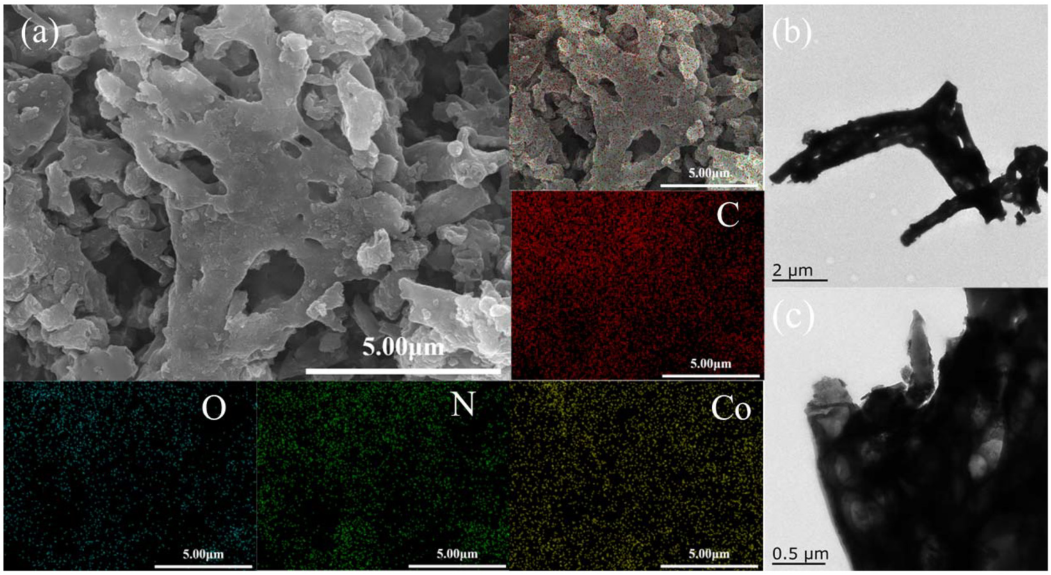

Fig. 3 (a) SEM images and elemental map of PCN-0.5Co. (b and c) TEM images of PCN-0.5Co.

The reduced electron penetrability and the absence of crystalline lattice fringes collectively imply a composite architecture that is weakly polymerized and predominantly amorphous in nature.[37]

The chemical composition and states of the elements present in PCN-M were investigated by X-ray photoelectron spectroscopy (XPS) (Fig. 4 and 5). The spectral analysis of PCN and PCN-M, as illustrated in Fig. 4a, indicates a significant

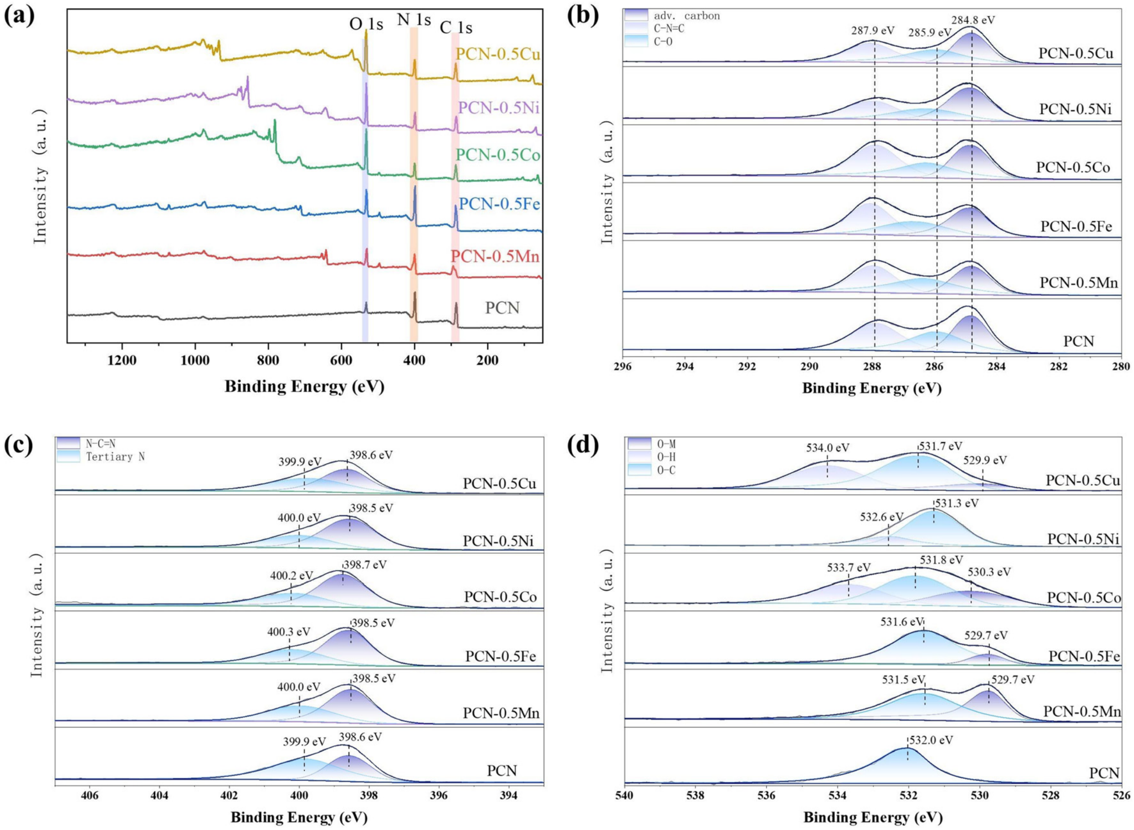

Fig. 4 XPS spectra of PCN and PCN-M: survey (a), C 1s (b), N 1s (c), and O 1s (d).

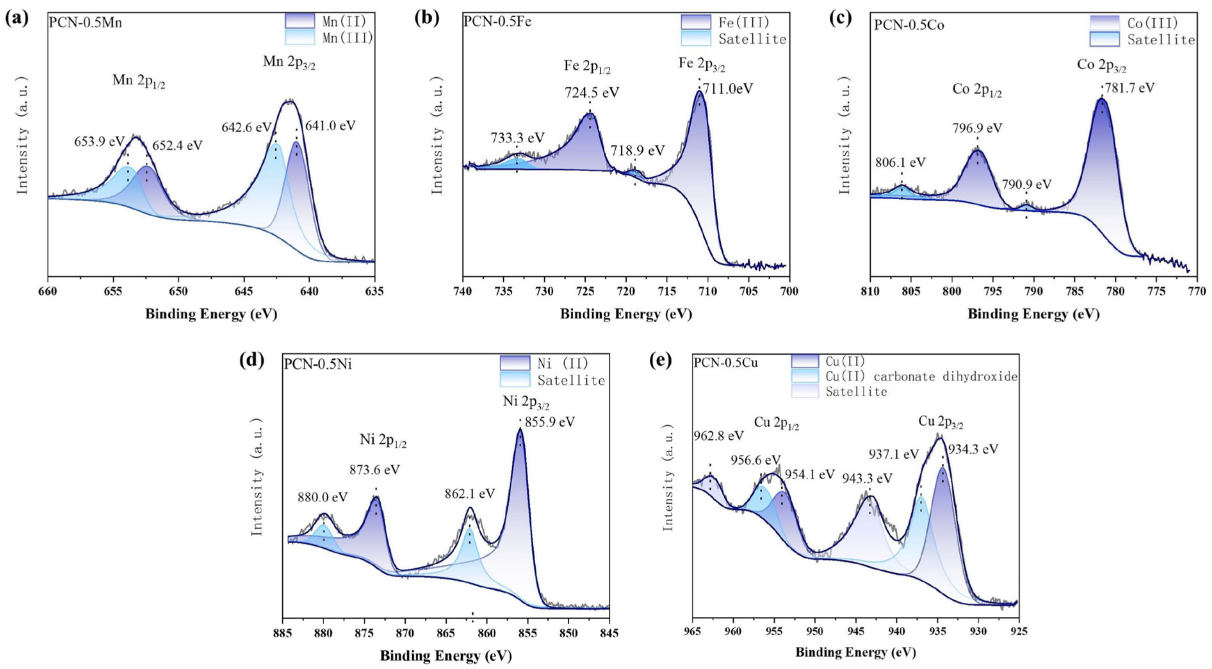

Fig. 5 XPS spectra of PCN-M: Mn 2p (a), Fe 2p (b), Co 2p (c), Ni 2p (d), and Cu 2p (e).

presence of carbon (286 eV), nitrogen (399 eV), and oxygen (530 eV), alongside minor metal signatures associated with the dopant species (M). The deconvolution of the C 1s peak of PCN (Fig. 4b) resulted in three different peaks centered at 284.8 eV, 285.9 eV, and 287.9 eV. The low energy peak (284.8 eV) could be attributed to the adventitious carbon, while the peaks at 285.9 eV and 287.9 eV could be attributed to the C–O bonds and sp^2-hybridized carbon in the C–N=C framework, respectively.[55] The C 1s spectral profiles of PCN-M composites are identical to those of PCN, suggesting that there are no metal–carbon coordination bonds present. For both PCN and PCN-M, the deconvolution of the N 1s peak resulted in two peaks centered at 398.6 and 400.0 eV (Fig. 4c). These peaks could be assigned to the N–C=N bonds (398.6 eV) and tertiary N–(C_3) (400.0 eV) in carbon nitride hetero-cycles.[56–59] The deconvolution of the O 1s peak of PCN resulted in a characteristic peak at 532.0 eV corresponding to the O–C bond.[57] PCN-M exhibit a consistent low-energy peak of this O–C bond, attributable to the introduction of an M–O bond from the metal oxide species. Distinctive O 1s peaks are observed at 533.7 eV (PCN-0.5Co) and 532.6 eV (PCN-0.5Ni), which are associated with surface hydroxyl groups (–OH).[60,61] In contrast, PCN-0.5Cu presents a broadened peak at around 534.0 eV, suggesting the presence of physically adsorbed oxygen species.[62]

Fig. 5a illustrates the Mn 2p peaks of PCN-0.5Mn, which can be deconvoluted into four distinct peaks: the peaks centered at 641.0 and 652.4 eV are associated with Mn(II), whereas the peaks centered at 642.6 and 653.9 eV indicate the presence of Mn(III). In the case of PCN-0.5Fe (Fig. 5b), the Fe 2p spectrum reveals characteristic peaks centered at 711.0 eV (Fe 2p$_{3/2}$) and 724.5 eV (Fe 2p$_{1/2}$) assigned to Fe(III), along with satellite peaks centered at 718.9 and 733.3 eV. The Co 2p spectrum for PCN-0.5Co (Fig. 5c) is resolved into four peaks, with those at 781.7 and 796.9 eV corresponding to Co(III), and satellite features at 790.9 and 806.1 eV.[63] Fig. 5d presents the Ni 2p spectrum of PCN-0.5Ni, showing dominant Ni(II) signatures at 855.9 eV (Ni 2p$_{3/2}$) and 873.6 eV (Ni 2p$_{1/2}$), with additional satellite peaks emerging at 862.1 and 880.0 eV.[64] Lastly, the Cu 2p spectrum of PCN-0.5Cu (Fig. 5e) is deconvoluted into six distinct components: peaks at 934.3 eV (Cu 2p$_{3/2}$) and 954.1 eV (Cu 2p$_{1/2}$) are attributed to Cu–O bonds in CuO, while features at 937.1 and 956.6 eV are associated with Cu(II) in basic copper carbonate. Satellite peaks at 943.3 and 962.8 eV further corroborate the divalent state of copper.[62]

3.2 Catalytic performance

Fig. 6 and Fig. S25–S34† show the DSC curves and derivative thermogravimetry (DTG) for pure AP and mixtures of PCN-M with AP. The introduction of 5 wt% PCN-0.5Co resulted in significant catalytic effects (Table S3†). Fig. 6b illustrates that PCN-0.5Co-modified AP shows merged LTD and HTD events as a single intensive exothermic peak centered at 296.32 °C, indicating synchronized thermal decomposition immediately following phase transition. This catalytic performance surpasses both PCN and other PCN-M composites, with the HTD temperature reduced by 125.71 °C compared to uncatalyzed AP. The accelerated decomposition kinetics confirms PCN-0.5Co's exceptional ability to lower activation energy barriers and promote complete oxidizer conversion.

TG-DSC analyses were performed to assess the catalytic effects of PCN-*x*Co composites on AP decomposition, by com-

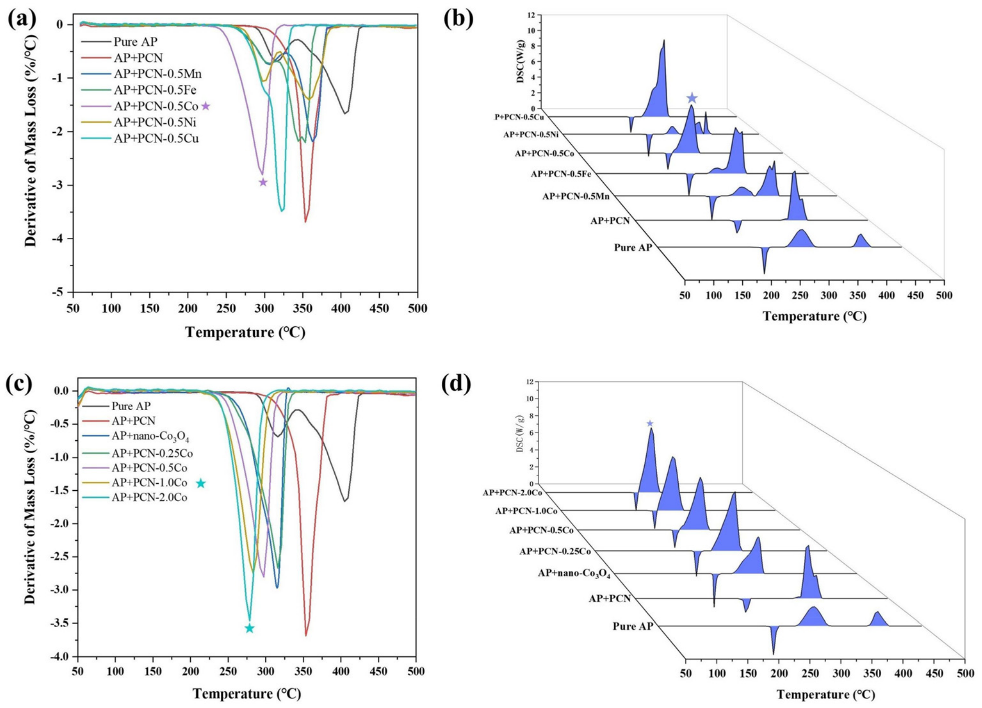

Fig. 6 (a) DTG results of pure AP, PCN, and PCN-M; (b) DSC results of pure AP, PCN, and PCN-M; (c) DTG results of pure AP, PCN, nano-Co_3O_4, and PCN-*x*Co; (d) DSC results of pure AP, PCN, nano-Co_3O_4, and PCN-*x*Co.

paring them with nano-Co_3O_4 (Fig. 6). Nano-Co_3O_4 showed significant catalytic activity, reducing AP's HTD peak temperature by 106.91 °C (exothermic enthalpy: 592.44 J g^{-1}). However, the PCN-*x*Co series exhibited even higher catalytic efficiency. Notably, the thermal decomposition of PCN-*x*Co-modified AP started simultaneously with its crystallographic phase transition. The catalytic performance was highly dependent on the Co content. As the Co loading increased from 0.25 to 2.00 mmol, the HTD temperatures decreased progressively by 104.43 °C, 125.71 °C, 138.86 °C, and 143.99 °C, respectively. Significantly, PCN-2.0Co achieved an HTD temperature lower than the LTD threshold of pristine AP, with a 49.2% reduction in decomposition duration and a 60.3% increase in enthalpy (949.99 J g^{-1}). This was a 35.1% greater reduction in HTD compared to nano-Co_3O_4, highlighting the structural advantages of carbon nitride-supported metal catalysts. These findings confirm PCN-2.0Co as a highly efficient AP decomposition catalyst. It outperforms conventional nanometal oxides due to synergistic electronic modulation and interfacial activation effects.

3.3 Catalytic mechanism

The activation energy (E_a) of AP thermal decomposition was determined through differential scanning calorimetry (DSC) measurements conducted at multiple heating rates. The thermal decomposition kinetics of AP formulations modified with 5 wt% PCN or PCN-M composites was investigated. As shown in Fig. 7, the exothermic peak temperatures during AP decomposition at varying heating rates were analyzed as a function of the heating rate using the Kissinger equation (eqn (1)) to derive critical kinetic parameters.

$$\ln\left(\frac{\beta}{{T_p}^2}\right) = -\frac{E_a}{RT_p} + \ln\left(\frac{AR}{E_a}\right) \tag{1}$$

where T_p is the peak decomposition temperature (K), β denotes the heating rate (K min^{-1}), E_a represents the apparent activation energy (kJ mol^{-1}), A is the pre-exponential factor, and R is the ideal gas constant (8.314 J (mol K)$^{-1}$). A linear relationship between $\ln(\beta/{T_p}^2)$ and $1/T_p$ allows the calculation of E_a and A from the slope and intercept, respectively (Fig. 7). The derived kinetic parameters for all systems are summarized in Table S4.†

Fig. 7a–g show the DSC curves of different AP formulations at various heating rates, and Fig. 7h and i display the corresponding Kissinger linear fittings. The activation energy (E_a) of pristine AP, calculated to be 270.43 kJ mol^{-1}, is consistent with literature values.[65–67] Notably, adding 5 wt% of PCN-M composites greatly changed the decomposition energetics. The E_a values of AP formulations modified by PCN, PCN-0.5Mn, PCN-0.5Fe, PCN-0.5Co, PCN-0.5Ni, and PCN-0.5Cu are 138.48, 230.13, 368.80, 113.04, 325.16, and 167.26 kJ mol^{-1}, respectively. Significantly, the E_a value of PCN-Co-catalyzed AP decomposition (113.04 kJ mol^{-1}) is close to that of the LTD stage of pristine AP, indicating an optimized catalytic pathway. Among all the catalysts, PCN-0.5Co shows the most significant E_a reduction, with a 58.20% decrease compared to pristine AP, outperforming both pristine PCN (with a 48.79% reduction) and other PCN-M variants. These kinetic results clearly

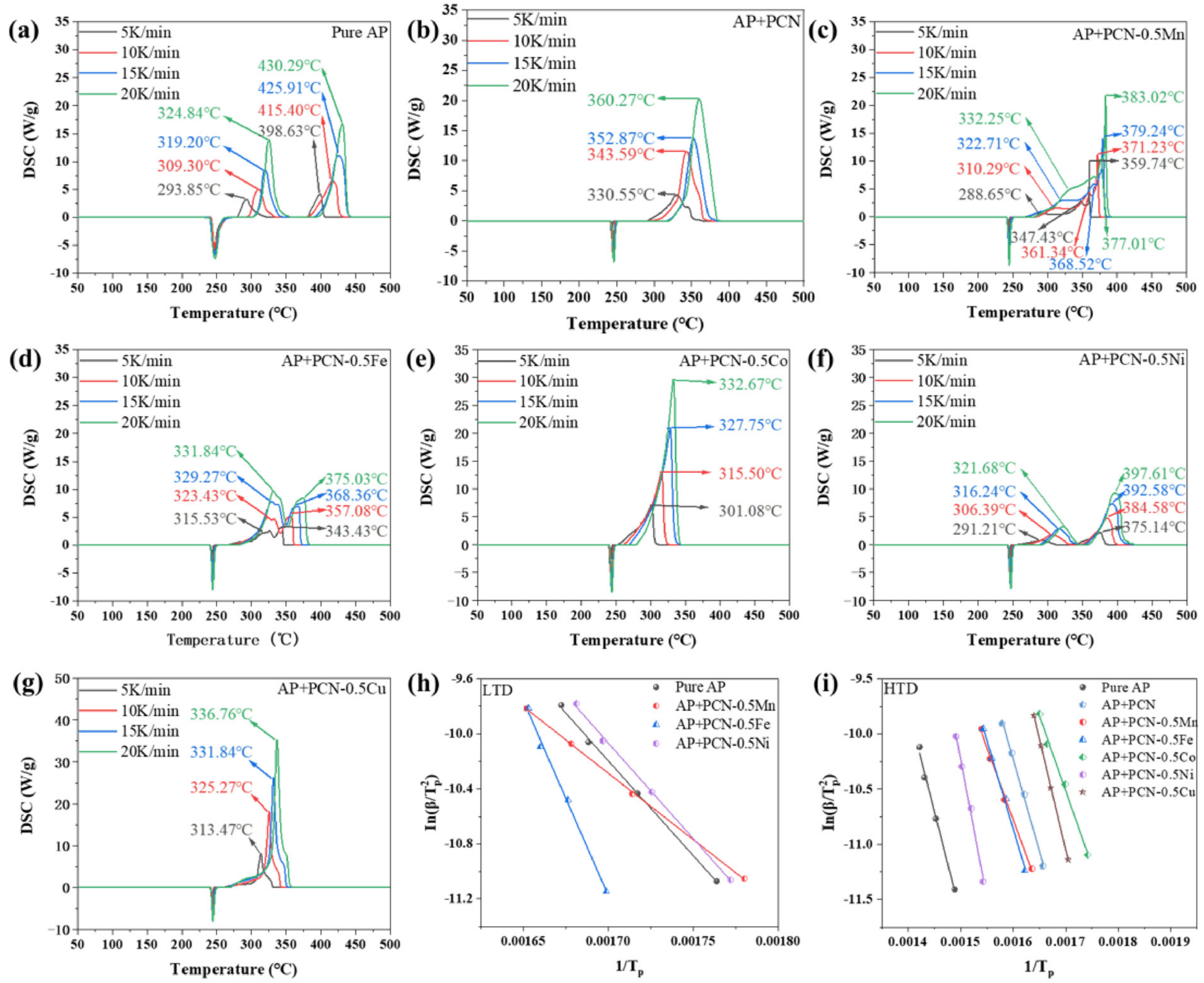

Fig. 7 DSC curves of pure AP (a), AP + PCN (b), AP + PCN-0.5Mn (c), AP + PCN-0.5Fe (d), AP + PCN-0.5Co (e), AP + PCN-0.5Ni (f), and AP + PCN-0.5Cu (g) at different heating rates; (h) $1/T_p$ and $\ln(\beta/T_p^2)$ fitting relationship of LTD for pure AP, PCN, and PCN-M; (i) $1/T_p$ and $\ln(\beta/T_p^2)$ fitting relationship of HTD for pure AP, PCN, and PCN-M.

confirm that PCN-0.5Co has superior catalytic efficiency in accelerating AP decomposition.

TG-FTIR monitored gaseous products during AP's catalytic decomposition to understand reaction pathways. Since NH_3 oxidizes to higher-valent nitrogen species, tracking N_2O, NO, and NO_2 is key to PCN-0.5Co's catalytic mechanism. Higher nitrogen oxidation states relate to more reactive O^-.[68] Fig. 8a shows the TG-FTIR results for pristine AP. Analyzing characteristic absorption bands and their temperature-dependent changes clearly resolves the LTD and HTD stages of AP decomposition. The key gaseous products are N_2O, NO, NO_2, NH_3, O_2, and H_2O, with nitrogen oxides dominant in the emission profile. Specific spectral assignments are 3400–3100 cm^{-1} for N–H (NH_3) and O–H (H_2O) stretching vibrations; 2400–2100 cm^{-1} for N≡N (N_2O) asymmetric stretching; 1670–1520 cm^{-1} for N–O (NO/NO_2) stretching modes; and 1340–1210 cm^{-1} for N═O (NO_2/N_2O) vibrations.[12,69,70]

FTIR spectra at exothermic peak temperatures were further analyzed to clarify the catalytic mechanism of PCN-0.5Co in AP decomposition. The generation and ratio of N_2O and NO are crucial in AP thermal decomposition. After the crystalline phase transition, proton transfer forms NH_3 and $HClO_4$ (eqn (2)). $HClO_4$ desorbs into the gas phase and decomposes step-by-step to generate reactive oxygen species (O^-). Then, NH_3 reacts with O^- to produce N_2O (eqn (3)), and N_2O further oxidizes to NO through O^--mediated reactions (eqn (4) and (5)).[71] Fig. 8 shows that temperature-resolved FTIR spectra distinguish the LTD and HTD processes of pristine AP. At 311 °C (LTD peak temperature), characteristic absorption bands at 2400–2100 cm^{-1} (N≡N) and 1340–1210 cm^{-1} (N═O) confirm N_2O generation. The lack of peaks in the 1670–1520 cm^{-1} region (N–O) indicates little NO/NO_2 production.[66] Limited O^- availability at this stage restricts $N_2O \rightarrow NO$ conversion, triggering a reverse reaction sequence ($N_2O \rightarrow NH_3 \rightarrow NH_4ClO_4$). $HClO_4$ desorbs more rapidly than NH_3, creating NH_3-saturated conditions. As a result, NH_3 adsorbs onto undecomposed AP particles. This surface passivation effect hinders subsequent decomposition reactions.[72] Thus, the HTD process requires a

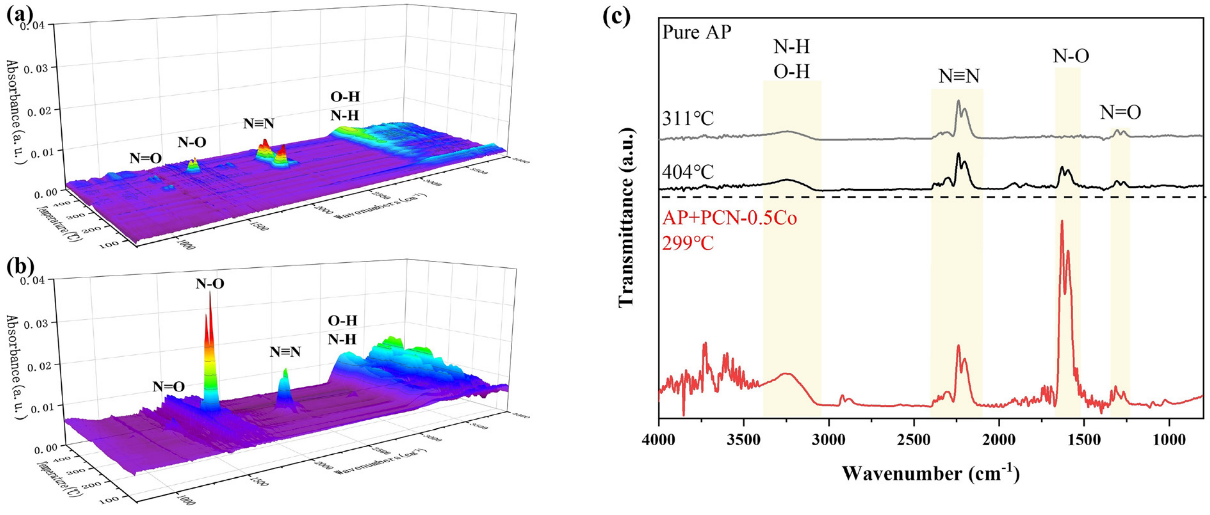

Fig. 8 (a) 3D TG-FTIR spectra of pure AP decomposition products; (b) 3D TG-FTIR spectra of decomposition products containing the PCN-0.5Co formulation; (c) FTIR spectra of decomposed gas products at different peaks at different temperatures.

higher activation energy (155.62 kJ mol^{-1}) than the LTD process (114.81 kJ mol^{-1}), as confirmed by the kinetic data in Table S4.† Rapid $HClO_4$ desorption relative to NH_3 creates NH_3-saturated conditions, leading to NH_3 adsorption on undecomposed AP particles. This surface passivation effect impedes subsequent decomposition reactions, necessitating higher activation energies for HTD progression (155.62 kJ mol^{-1}) compared to LTD (114.81 kJ mol^{-1}), as corroborated by kinetic data in Table S4.†

$$NH_4ClO_4 \rightarrow NH_4{}^+ + ClO_4{}^- \leftrightarrow NH_3\ (g) + HClO_4\ (g) \quad (2)$$

$$HClO_4\ (g) \rightarrow ClO_3 + ClO + O_2 + H_2O \quad (3)$$

$$O_2 + e^- \rightarrow O_2{}^- \quad (4)$$

$$NH_3 + O_2{}^- \rightarrow O + NO_2 + H_2O + e^- \quad (5)$$

At 404 °C (HTD peak) for pristine AP, FTIR analysis detected absorption peaks in the 2400–2100 cm^{-1} (N≡N), 1670–1520 cm^{-1} (N–O), and 1340–1210 cm^{-1} (N═O) regions, confirming the generation of N_2O, NO, and NO_2. At this stage, adsorbed NH_3 desorbs from AP particles, allowing gas-phase reactions between NH_3 and $HClO_4$ decomposition products to produce N_2O, NO, O_2, and NO_2.[73] For the AP + PCN-0.5Co system at 299 °C (HTD peak), the FTIR spectrum showed a notably stronger N–O band (1670–1520 cm^{-1}) than that of pristine AP at 404 °C. Quantitative analysis revealed a higher N–O : N≡N peak ratio (1.66 for AP + PCN-0.5Co *vs.* 0.60 for pristine AP).

Based on experimental results, the catalytic mechanism of PCN-0.5Co is proposed as follows (Fig. 9). The PCN matrix is coated with Lewis-basic CoO(OH) on its surface. During proton-transfer reactions, $HClO_4$ adsorbs onto PCN-0.5Co through Lewis acid–base interactions.[74] This separates $HClO_4$ molecules from AP pores, reducing the activation energy and accelerating the LTD process.[47] CoO(OH) has numerous lattice defects (h^+/e^- pairs). These defects react with adsorbed $HClO_4$ to generate reactive oxygen radicals (O^-), which promote the oxidation of NH_3 to higher-valent nitrogen species (NO/NO_2).[75] The large specific surface area of PCN-0.5Co enhances gas-molecule adsorption, speeds up reaction kinetics, and exposes more active sites, thus intensifying AP decomposition.[20,76] In addition to these active sites, the presence of partially filled 3d orbitals of Co atoms, gaseous NH_3 molecules will easily get adsorbed onto the catalyst surface and form coordination compounds with the Co atom.[74] Additionally, the conductive PCN framework enables rapid electron transfer during thermal decomposition. This ensures that charge carriers fully participate in redox reactions and lower the threshold temperature for complete AP decomposition.

3.4 Propellant combustion performance

Fig. 10a shows the morphology and particle size distribution of AP used in this study. Fig. 10b presents the cross-sectional SEM images and corresponding EDS elemental maps of HTPB-based solid propellants with 2 wt% PCN-2.0Co. Highly plasticized HTPB macromolecules form a continuous polymeric network, encapsulating AP particles and spherical aluminum powder, leading to a densely packed propellant grain. The composite has a uniform dispersion of components, strong interfacial bonding, and few voids. EDS elemental mapping verifies the homogeneous distribution of Co, O, Al, Cl, and N on the spherical particle surfaces (Fig. 10b). Fig. 10c and d display the DTG and DSC profiles of HTPB-based solid propellants with different catalysts. For the baseline (uncatalyzed) formulation, decomposition occurs in three stages. The LTD stage (270–320 °C) mainly involves AP decomposition, with a 15% mass loss. The HTD stage (320–390 °C) is dominated by the simultaneous decomposition of AP and HTPB macro-

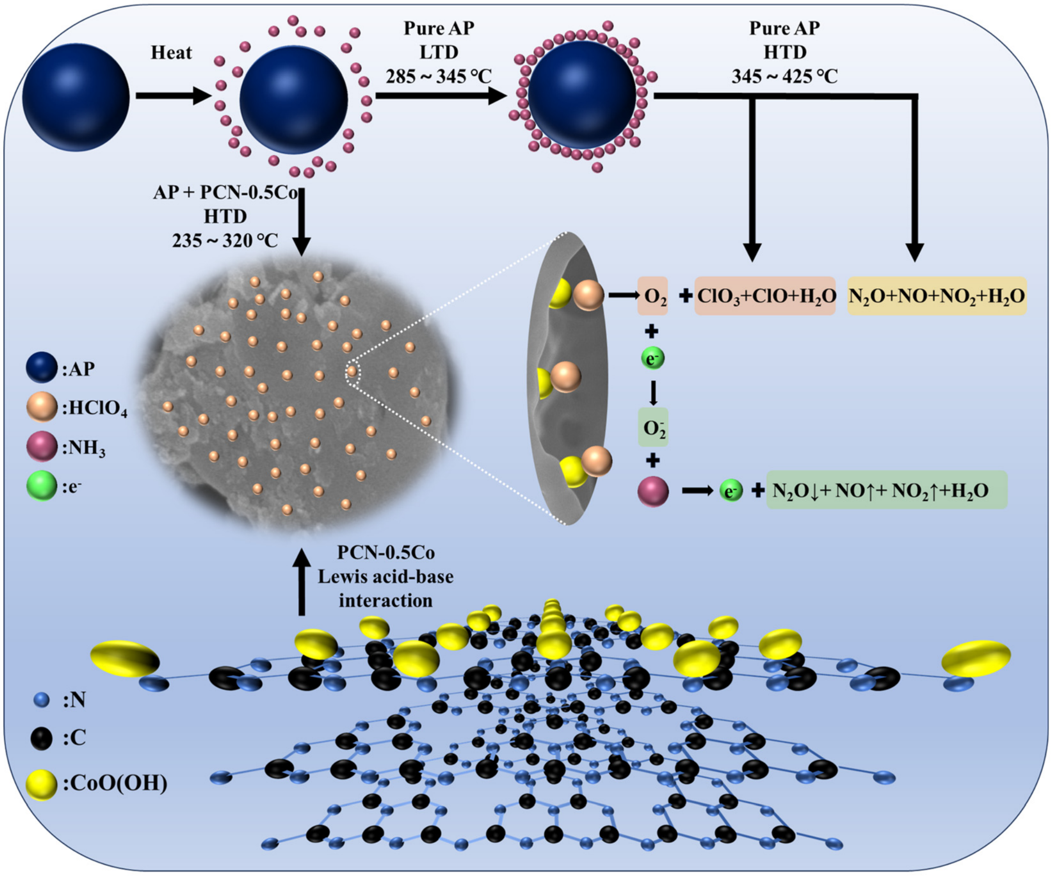

Fig. 9 Schematic diagram of the mechanism of PCN-0.5Co promoting thermal decomposition of AP.

molecules, resulting in 50% mass loss and most of the exothermic activity. The residual decomposition (420–480 °C) is due to the remaining HTPB degradation (7% mass loss), with no distinct exothermic peaks as the heat release is minimal. As shown in Table S6,† the exothermic peaks for the LTD and HTD stages are at 300.10 °C and 380.68 °C, respectively, in line with the staged-decomposition mechanism.

The HTPB-based solid propellant with PCN-2.0Co showed enhanced decomposition. The DTG curve had a rapid mass loss in a narrow temperature range, and the DSC profile had a distinct exothermic peak. In contrast, ferrocene-derivative-modified propellants had merged decomposition stages over broad temperature ranges ($\Delta T > 80$ °C) with dispersed exothermic activity. Uncatalyzed propellants and those modified with nano-Co_3O_4, the PCN precursor, or pristine PCN all had two clear exothermic stages. Significantly, the PCN-2.0Co-modified propellant had the lowest HTD temperature of 327.17 °C, 53.51 °C lower than the baseline (380.68 °C), along with a more concentrated exothermic release.

As shown in Table S6,† different catalysts impact the density of HTPB-based solid propellants. Nano-scale catalysts notably increase the propellant density. When PCN-2.0Co composites and nano-Co_3O_4 are added, the explosion heat of the corresponding propellants reaches 4996 J g^{-1} and 5015 J g^{-1} respectively, significantly improving their energy performance. BAM-method impact and friction sensitivity tests indicated that adding PCN-2.0Co reduces the sensitivity of HTPB-based propellants.

The combustion characteristics of propellants are crucial for determining the thrust output of rocket engines. Combustion experiments were carried out under atmospheric pressure using a constant current ignition system. The solid propellant, fixed in a mold with 2 cm incremental markers, was ignited, and the combustion process was recorded at 60 frames per second. Burning rates were calculated by measuring the time intervals as the flame front passed successive markers. Combustion interfaces were photographed every 20 seconds to generate flame propagation distance profiles (Fig. 11 and Fig. S38†).

When 2 wt% of PCN-2.0Co composites were incorporated into HTPB-based solid propellants, the burning rate was significantly enhanced. Specifically, it surged from the baseline value of 0.972 mm s^{-1} to 1.355 mm s^{-1}, representing a substantial 39.40% increase. In contrast, for the comparative systems modified with ferrocene derivatives,[77] nano-Co_3O_4,[78] and the PCN precursor,[39] the improvements in the burning rate were markedly lower. They were 4.21% (resulting in a rate

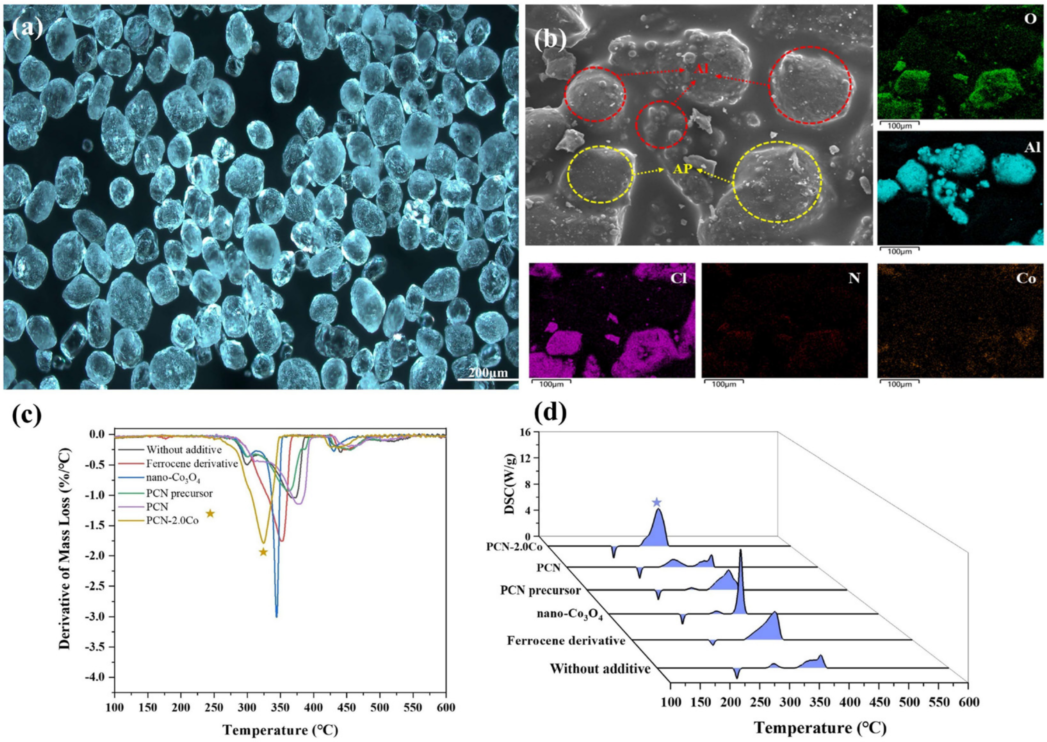

Fig. 10 (a) AP micrograph; (b) SEM image and elemental map of the solid propellant with PCN-2.0Co added; (c) DTG diagram of the HTPB-based solid propellant with different types of catalysts under a N_2 atmosphere; (d) DSC diagram of the HTPB-based solid propellant with different types of catalysts under a N_2 atmosphere.

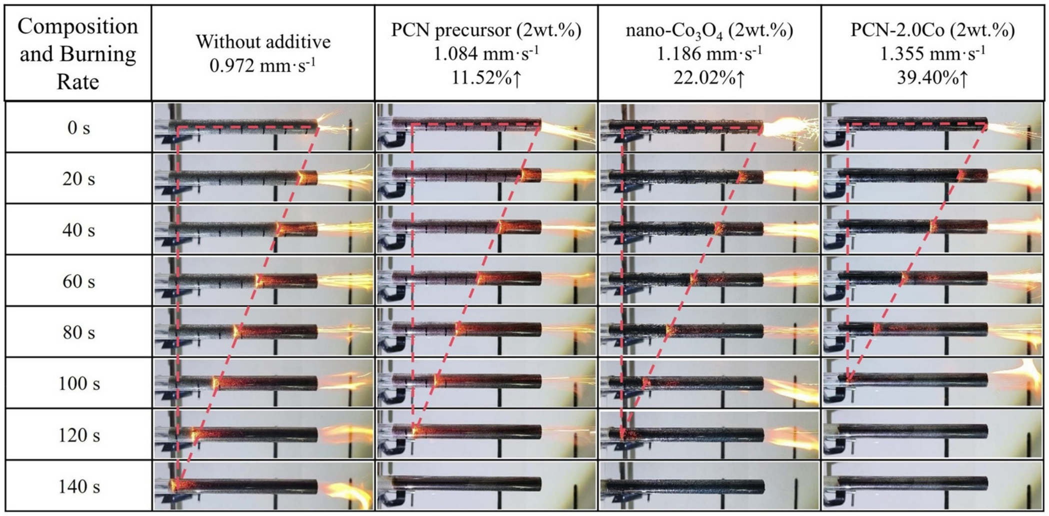

Fig. 11 Selected images of the HTPB-based solid propellant burning under atmospheric conditions without additives and with the addition of the PCN precursor (2 wt%) and PCN-2.0Co (2 wt%).

of 1.013 mm s^{-1}), 22.02% (1.186 mm s^{-1}), and 11.52% (1.084 mm s^{-1}), respectively. The propellant modified by PCN-2.0Co manifested intensified combustion behavior. It was characterized by concentrated flame fronts and increased luminosity, which indicated optimized combustion efficiency.

4. Conclusions

In this study, CoO(OH)/polymeric carbon nitride (PCN-0.5Co) composites were successfully synthesized through a rapid low-temperature calcination method, presenting a revolutionary approach to boost the thermal decomposition efficiency of AP in solid propellants. The optimized PCN-0.5Co catalyst notably reduces AP's HTD temperature by 125.71 °C and cuts the activation energy by 58.2% to 113.04 kJ mol^{-1}, outperforming traditional catalysts such as nano-Co_3O_4. Mechanistic investigations indicate that the synergy between CoO(OH) and PCN promotes $HClO_4$ adsorption *via* Lewis acid–base interactions and generates reactive oxygen species (O_2^-), thereby accelerating the oxidation of NH_3 to NO/NO_2. When 2 wt% of PCN-2.0Co is incorporated into HTPB-based propellants, the thermal decomposition process is consolidated into a single exothermic peak. The HTD temperature is decreased by 53.51 °C, the combustion rate is increased by 39.4% to 1.355 mm s^{-1}, and the energy density is elevated to 4996 J g^{-1}. This study firmly establishes PCN-0.5Co as a high-performance catalyst for AP-based propulsion systems and significantly advances the application of carbon nitride composites in energetic materials.

Author contributions

Qin Liu: writing – original draft, visualization, validation, methodology, investigation, data curation, and conceptualization. Siyu Ma: writing – review & editing, supervision, resources, project administration, funding acquisition, and formal analysis. Xingyang Cui: validation, methodology, investigation, and conceptualization. Shuyue Xu: validation and methodology. Jinchao Ma: supervision and funding acquisition. Hua Qian: supervision and funding acquisition.

Conflicts of interest

The authors declare that they have no known competing financial interests or personal relationships that could have appeared to influence the work reported in this paper.

Data availability

The data supporting this article have been included as part of the ESI.†

Acknowledgements

This work was supported by the National Natural Science Foundation of China (grant no. 22305122), the Natural Science Foundation of Jiangsu Province (grant no. BK20230935), the Innovation Foundation of Shanghai Academy of Spaceflight Technology (grant no. SAST2021-014 and SAST2023-079), and the China National Key Laboratory of Energetic Materials. The authors extend their gratitude to Shiyanjia Lab (**https://www.shiyanjia.com**) for providing the exact test with the SEM and XPS analyses.

References

1 S. Chaturvedi and P. N. Dave, *Arabian J. Chem.*, 2019, **12**, 2061–2068.

2 C. M. Grégoire, O. Mathieu, J. Kalman and E. L. Petersen, *Prog. Energy Combust. Sci.*, 2025, **106**, 101195.

3 T. Chen, Y. Hu, C. Zhang and Z. Gao, *Def. Technol.*, 2021, **17**, 1471–1485.

4 M. Kohga, R. Togashi, H. Tsutiya and Y. Ota, *Combust. Flame*, 2022, **246**, 112459.

5 R. Li, X. Li, G. Yang, C. Guo, L. Zhang, C. Hao and W. Zhu, *Appl. Surf. Sci.*, 2023, **615**, 156349.

6 C. Dennis and B. Bojko, *Fuel*, 2019, **254**, 115646.

7 M. Nourine, M. K. Boulkadid, S. Touidjine, H. Akbi and S. Belkhiri, *Mater. Chem. Phys.*, 2023, **303**, 127784.

8 X. Liu, X. Ma, G. Wang and Z. Chen, *Fuel*, 2024, **375**, 132440.

9 H. Luo, J. Chen, J. Wang, S. Li, X. Li and J. Yang, *Fuel*, 2025, **379**, 133122.

10 P. N. Dave and R. Sirach, *Mater. Sci. Eng., B*, 2024, **301**, 117136.

11 C. Feng, B. Ye, W. Cheng, S. Shi, F. Zhao, C. An and J. Wang, *Case Stud. Therm. Eng.*, 2024, **56**, 104281.

12 J. A. Vara, P. N. Dave and S. Chaturvedi, *Def. Technol.*, 2019, **15**, 629–635.

13 T. An, W. He, S.-W. Chen, B.-L. Zuo, X.-F. Qi, F.-Q. Zhao, Y. Luo and Q.-L. Yan, *J. Phys. Chem. C*, 2018, **122**, 26956–26964.

14 D. L. Reid, A. E. Russo, R. V. Carro, M. A. Stephens, A. R. LePage, T. C. Spalding, E. L. Petersen and S. Seal, *Nano Lett.*, 2007, **7**, 2157–2161.

15 S. Chaturvedi and P. N. Dave, *J. Exp. Nanosci.*, 2012, **7**, 205–231.

16 J. A. Vara, P. N. Dave and S. Chaturvedi, *Combust. Sci. Technol.*, 2021, **193**, 2290–2304.

17 X. Li, Y. Zhang, R. Xu, Q.-L. Yan and H. Nie, *ACS Appl. Mater. Interfaces*, 2025, **17**, 37150–37161.

18 B. Ye, W. Li, Y. Tang, C. An and J. Wang, *Vacuum*, 2024, **228**, 113495.

19 H. Fang, R. Xu, L. Yang, Z. Mi, Q. He, H. Shi, L. Jiang, X. Fu and G. Zhang, *J. Alloys Compd.*, 2022, **928**, 167134.

20 L.-N. Jin, Q. Liu and W.-Y. Sun, *CrystEngComm*, 2012, **14**, 7721.

21 J. Pei, H. Zhao, F. Yang and D. Yan, *Langmuir*, 2021, **37**, 6132–6138.

22 E. Alizadeh-Gheshlaghi, B. Shaabani, A. Khodayari, Y. Azizian-Kalandaragh and R. Rahimi, *Powder Technol.*, 2012, **217**, 330–339.

23 Y. Sun, Y. Zhu, S. Zhang, S. Chen, F. Zhao and K. Xu, *Ceram. Int.*, 2024, **50**, 43617–43626.

24 H. Li, Q. Cai, H. Li, S. Zeng, S. Shi, W. Xu, R. Wang, C. Luo and Y. Liu, *Ceram. Int.*, 2025, **51**, 20433–20443.

25 J. Chen, L. Zhang, J. Sun, J. Zhu, X. Wang and Y. Fu, *Appl. Surf. Sci.*, 2022, **571**, 151342.

26 Y. Yuan, W. Jiang, Y. Wang, P. Shen, F. Li, P. Li, F. Zhao and H. Gao, *Appl. Surf. Sci.*, 2014, **303**, 354–359.

27 J. Xu, S. Li, L. Tan and B. Kou, *Mater. Res. Bull.*, 2017, **93**, 352–360.

28 K. Li, Y. Lei, J. Liao, S. Huang, Y. Zhang and W. Zhu, *Ceram. Int.*, 2021, **47**, 33269–33279.

29 K. Li, Y. Lei, J. Liao and Y. Zhang, *Inorg. Chem. Front.*, 2021, **8**, 1747–1761.

30 P. Deng, Q. Jiao and H. Ren, *J. Mater. Sci.*, 2021, **56**, 2077–2087.

31 N. Li, Z. Geng, M. Cao, L. Ren, X. Zhao, B. Liu, Y. Tian and C. Hu, *Carbon*, 2013, **54**, 124–132.

32 H. Akbi, S. Rafai, A. Mekki, S. Touidjine, M. Fertassi and D. E. Kadri, *J. Organomet. Chem.*, 2022, **957**, 122159.

33 Q. Luo, X. Chang, Z. Cheng, Y. Qiu, G. Tan and M. Chen, *J. Organomet. Chem.*, 2024, **1022**, 123401.

34 P. Chandrababu, J. Thankarajan, V. Sukumaran Nair and R. Raghavan, *Thermochim. Acta*, 2020, **691**, 178720.

35 J. Wang, Y. Li, H. Wang, T. Tian, S. Zhu, J. Zhou, X. Wu and W. Qin, *Eur. J. Inorg. Chem.*, 2017, **2017**, 3154–3160.

36 E. An, X. Li, C. Yu, Y. Tan, Z. Fan, Q. Li, P. Deng and X. Cao, *Def. Technol.*, 2024, **31**, 288–294.

37 Y. Zhang, K. Li, J. Liao, X. Wei and L. Zhang, *Appl. Surf. Sci.*, 2020, **499**, 143875.

38 C. Zhang, X. Yang, Z. Zhang, J. Li, W. Jin and H. Ma, *Surf. Interfaces*, 2022, **35**, 102425.

39 J. Ma, J. Das, J. Zhang, J. Cheng, S. Sorcar, B. A. Rosen, P. Shekhter, R. Dobrovetsky, E. Flaxer, Y. Yavor, R. Shen, I. Kaminker, A. Goldbourt and M. Gozin, *Small*, 2023, **19**, 2205994.

40 J. Dai, J. H. Huang, L. F. Gao, Z. K. Qi and K. F. Chen, *Microchem. J.*, 2025, **212**, 113272.

41 M. M. Rahman, F. Azim, A. A. Sijuade, N. Anjum, S. R. Mishra and O. Okoli, *J. Alloys Compd.*, 2025, **1016**, 178821.

42 Y. Han, C. Guo, G. Li, P. Lv, Y. Zhang, T. Jiang, T. Ma, N. Wang, Y. Yin, Y. Liu and X. Yin, *Surf. Interfaces*, 2025, **59**, 105965.

43 S. K. Sharma, Kavyashree, P. Maurya and S. N. Pandey, *J. Energy Storage*, 2024, **79**, 110140.

44 H. Zhang, Z. Bian, S. Zhang, H. Li, W. Li, Z. Mao, H. Yin, H. Zhang, G. Wang and Y. Zhang, *SSRN*, 2025, preprint, DOI: 10.2139/ssrn.5180193.

45 M. O. Farea, E. Alzahrani, T. M. Alresheedi, A. N. Al-Hakimi, N. Y. Elamin, L. A. M. Al-sagheer, G. M. Asnag and D. Abdelhameed, *Inorg. Chem. Commun.*, 2025, **180**, 114954.

46 Y. Zhou, L. Zhang, J. Liu, X. Fan, B. Wang, M. Wang, W. Ren, J. Wang, M. Li and J. Shi, *J. Mater. Chem. A*, 2015, **3**, 3862–3867.

47 Q. Li, Y. He and R. Peng, *RSC Adv.*, 2015, **5**, 24507–24512.

48 J. Xu, L. Zhang, R. Shi and Y. Zhu, *J. Mater. Chem. A*, 2013, **1**, 14766.

49 T. Y. Ma, Y. Tang, S. Dai and S. Z. Qiao, *Small*, 2014, **10**, 2382–2389.

50 H. Xu, J. Yan, Y. Xu, Y. Song, H. Li, J. Xia, C. Huang and H. Wan, *Appl. Catal., B*, 2013, **129**, 182–193.

51 Q. Xiang, J. Yu and M. Jaroniec, *J. Phys. Chem. C*, 2011, **115**, 7355–7363.

52 P. He, L. Song, S. Zhang, X. Wu and Q. Wei, *Mater. Res. Bull.*, 2014, **51**, 432–437.

53 S. C. Yan, Z. S. Li and Z. G. Zou, *Langmuir*, 2009, **25**, 10397–10401.

54 K. H. Leong, S. L. Liu, L. C. Sim, P. Saravanan, M. Jang and S. Ibrahim, *Appl. Surf. Sci.*, 2015, **358**, 370–376.

55 Y. Chen, W. Huang, D. He, Y. Situ and H. Huang, *ACS Appl. Mater. Interfaces*, 2014, **6**, 14405–14414.

56 X. Ji, B. Xu, H. Zhang, X. Xia, K. Ji, A. Szymska, K. Matras-Postolek and P. Yang, *ACS Appl. Nano Mater.*, 2022, **5**, 11731–11740.

57 J. A. Singh, S. H. Overbury, N. J. Dudney, M. Li and G. M. Veith, *ACS Catal.*, 2012, **2**, 1138–1146.

58 J. Zhang, M. Zhang, G. Zhang and X. Wang, *ACS Catal.*, 2012, **2**, 940–948.

59 S. J. Yang, J. H. Cho, G. H. Oh, K. S. Nahm and C. R. Park, *Carbon*, 2009, **47**, 1585–1591.

60 J. Zhang, S. Shao, D. Zhou, T. Di and T. Wang, *ACS Appl. Energy Mater.*, 2021, **4**, 6340–6347.

61 S. Chen, W. Wang, Y. Hou, Y. Hao, Y. Zhao, S. Wang, J. Meng and H. Xu, *ACS Appl. Nano Mater.*, 2023, **6**, 8717–8725.

62 A. K. Rathi, H. Kmentová, A. Naldoni, A. Goswami, M. B. Gawande, R. S. Varma, Š. Kment and R. Zbořil, *ACS Appl. Nano Mater.*, 2018, **1**, 2526–2535.

63 A. Firoozbakhtian, B. Salah, K. Eid, M. Hosseini and G. Xu, *Langmuir*, 2024, **40**, 3260–3267.

64 B. Dong, M. Li, S. Chen, D. Ding, W. Wei, G. Gao and S. Ding, *ACS Appl. Mater. Interfaces*, 2017, **9**, 17890–17896.

65 M. R. Sovizi, G. Fakhrpour and A. R. Madram, *J. Therm. Anal. Calorim.*, 2017, **129**, 401–410.

66 R. Yang, Y. Kou, J. Wei, Q. Lu, W. Zhang, Z. Chen, C. Zhang, H. Gao, F. Zhao, W. Jiang and G. Hao, *Int. Commun. Heat Mass Transfer*, 2025, **160**, 108358.

67 G. Zhang, X. Yu, Z. Wang, S. Li, Z. Zhao, Y. Zhu, Z. Yan, G. Chen and X. Xiao, *Carbon*, 2023, **215**, 118484.

68 P. Zhou, X. Tang, Z. Ren, Z. Zheng, K. Zhang, R. Zhou, D. Wu, J. Liao, Y. Zhang and C. Huang, *Small*, 2023, **19**, 2207023.

69 D. Ma, X. Li, X. Wang and Y. Luo, *RSC Adv.*, 2021, **11**, 5729–5740.

70 N. M. Juibari and S. Tarighi, *J. Alloys Compd.*, 2020, **832**, 154837.

71 J. Han, S. Hu and L. Liu, *Def. Technol.*, 2024, **35**, 174–186.

72 Y. Zhu, S. Dong, Y. Zhang, L. Cui, S. Chen, F. Zhao and K. Xu, *Chem. Eng. J.*, 2025, **514**, 163071.

73 G. Zhang, X. Yu, Z. Wang, S. Li, Z. Zhao, Y. Zhu, Z. Yan, G. Chen and X. Xiao, *Carbon*, 2023, **215**, 118484.

74 G. Mani, P. R. Nair and S. Mathew, *Next Res.*, 2025, **2**, 100203.

75 L.-Y. Zhou, S.-B. Cao, L.-L. Zhang, G. Xiang, X.-F. Zeng and J.-F. Chen, *ACS Appl. Mater. Interfaces*, 2022, **14**, 3476–3484.

76 L. Zhou, S. Cao, L. Zhang, G. Xiang, J. Wang, X. Zeng and J. Chen, *J. Hazard. Mater.*, 2020, **392**, 122358.

77 J. Liu, Y. Zhang, H. Yu, L. Wang, S. Z. Vatsadze, D. Chen and C. Ouyang, *Appl. Organomet. Chem.*, 2023, **37**, e7292.

78 Y. Zhu, X. Yu, G. Zhang, Z. Yan and X. Xiao, *J. Phys. Chem. Solids*, 2023, **182**, 111580.